Dosimetric impact of a CT metal artefact suppression algorithm for proton, electron and photon therapies

Dosimetric impact of a CT metal artefact suppression algorithm for proton, electron and photon therapies

Jikun Wei[1]**, George A Sandison**[1]**, Wen-Chien Hsi**[2]**, Michael Ringor**[3]
and Xiaoyi Lu[4]

[1] School of Health Sciences, Purdue University, 550 Stadium Mall Drive, West Lafayette,
IN 47907, USA
[2] Midwest Proton Radiotherapy Institute, 2425 Milo B Sampson Road, Bloomington, IN 47408,
USA
[3] Faith, Hope and Love Cancer Care, Unity HealthCare, 1345 Unity Place, Lafayette, IN 47905,
USA
[4] Department of Radiation Oncology, Indiana University Medical School, Indianapolis,
IN 46202, USA

Abstract
Accurate dose calculation is essential to precision radiation treatment planning
and this accuracy depends upon anatomic and tissue electron density
information. Modern treatment planning inhomogeneity corrections use x-
ray CT images and calibrated scales of tissue CT number to electron density to
provide this information. The presence of metal in the volume scanned by an x-
ray CT scanner causes metal induced image artefacts that influence CT numbers
and thereby introduce errors in the radiation dose distribution calculated.
This paper investigates the dosimetric improvement achieved by a previously
proposed x-ray CT metal artefact suppression technique when the suppressed
images of a patient with bilateral hip prostheses are used in commercial
treatment planning systems for proton, electron or photon therapies. For all
these beam types, this clinical image and treatment planning study reveals that
the target may be severely underdosed if a metal artefact-contaminated image
is used for dose calculations instead of the artefact suppressed one. Of the three
beam types studied, the metal artefact suppression is most important for proton
therapy dose calculations, intermediate for electron therapy and least important
for x-ray therapy but still significant. The study of a water phantom having
a metal rod simulating a hip prosthesis indicates that CT numbers generated
after image processing for metal artefact suppression are accurate and thus
dose calculations based on the metal artefact suppressed images will be of high
fidelity.

(Some figures in this article are in colour only in the electronic version)

1. Introduction

To correctly calculate dose distribution in the presence of tissue inhomogeneities modern treatment planning systems require a 3D matrix of x-ray CT-derived tissue electron density values in every voxel in and about the volume of interest. This information is obtained from x-ray CT images by calibration and conversion of Hounsfield units (HU) assigned to voxels of the images into tissue electron density values. Several authors have discussed this calibration process and how the CT numbers can be used for inhomogeneity correction in treatment planning (Goitein 1978, Parker *et al* 1979, Perry and Holt 1980, Henson and Fox 1994, Thomadsen *et al* 1983, Constantinou *et al* 1992, Schneider *et al* 1996, Guan *et al* 2002). However, a commonly encountered clinical problem is that the presence of metal in the volume scanned by the x-ray CT scanner induces metal artefacts in the resulting CT images leading to wrong electron density values for the patient tissue within the 3D matrix. Ultimately, dose calculations that utilize these wrong values predict erroneous radiation dose distributions within the patient.

Mustafa and Jackson (1983) discussed the relation between relative CT number values and charged particle stopping powers and their significance for radiotherapy treatment planning. More recently, CT calibration for the accurate calculation of proton beam propagation in inhomogeneous media has been discussed (Szymanowski and Oelfke 2003). It has long been recognized that x-ray CT-based treatment planning is compromised by patient metal implants and this problem has been discussed by many authors (Coolens and Childs 2003, Roberts 2001, Wieslander and Knoos 2003, Ding and Yu 2001). Roberts (2001) studied the accuracy of a treatment planning pencil beam algorithm for 6 MV and 15 MV x-rays for a patient with metal implants. He compared the experimental measurements to the CT-based treatment planning system (TPS) results and found dose errors over 10%. Ding and Yu (2001) performed a comparison between Monte Carlo photon beam dose calculations and a commercial TPS (CADPLAN) and found dose errors of 15%. Wieslander and Knoos (2003) compared Monte Carlo dose calculations for photon beams passing through metal implants to those generated by two common algorithms in commercial TPSs, the pencil beam (PB) algorithm and the collapsed cone (CC) algorithm. They found the CC algorithm more accurate than the PB one when beams pass through metal implants before reaching the planning tumour volume (PTV). Coolens and Childs (2003) investigated the possible use of the extended CT scale in the calibration of CT Hounsfield units for treatment planning of patients with metallic hip prostheses and found that both of the two available methods, the material substitution method and the stoichiometric calibration method, failed to successfully predict the electron densities for the metallic hip prostheses.

All of the previous studies considered radiation beams passing through the metallic implants. However treatment planners, knowing that dosimetric predictions are unreliable in such situations, do their best to avoid direct irradiation of metal implants by arranging treatment beams appropriately. Even though the metal objects are avoided along the beam path, the CT-calibrated inhomogeneity correction in dose calculation is still compromised by the sometimes severe CT metal artefacts overlapping body tissues in the image. Therefore a more clinically relevant question is, how accurate is treatment planning in the presence of CT metal artefacts and will CT metal artefact suppression techniques improve treatment planning accuracy?

We recently have proposed a novel metal artefact suppression technique for CT images, named the smoothing-plus-scaling technique (Wei *et al* 2004). The suppression technique is a general one that improves CT images regardless of the origin of the metal artefact (e.g. metal on immobilization devices external to the patient, metal amalgam dental fillings, metal

brachytherapy intracavitary devices, implanted metal cryotherapy probes etc). This paper investigates the dosimetric impact of this x-ray CT metal artefact suppression technique on dose calculations generated by commercial treatment planning systems for proton, electron and photon beams. A patient with bilateral hip prostheses was chosen as the example subject. To analyse the CT number accuracy after the artefact suppression processing procedure, a water phantom with a metal rod simulating a hip prosthesis was CT scanned, processed and analysed.

This paper is organized as follows. In section 2 the investigation method is outlined. In section 3 x-ray CT number accuracy is analysed after implementing the CT metal artefact suppression technique. Sections 4, 5 and 6 discuss the clinical studies to demonstrate the dosimetric impact of the metal artefact suppression technique for proton, electron and photon beams, respectively. Conclusions are provided in section 7

2. Method

After applying the metal artefact suppression algorithm, CT numbers of the dark streaks overlapping with tissues in the artefact-contaminated images are increased while the CT numbers of bright streaks are decreased. It is hypothesized that these altered CT numbers are close to the CT numbers of the same anatomical region that would be produced in a metal-free image and any differences will have only a small perturbation of the calculated dose distribution in soft tissue. To test the hypothesis, a water phantom with and without a metal rod placed in it was CT scanned. The images of the metal rod were processed by the artefact suppression algorithm. The CT numbers in the metal-free image, metal artefact-contaminated image and the artefact-suppressed image were mathematically compared by calculating the mean and standard deviations of the difference images obtained by subtracting the artefact-suppressed image from the artefact-contaminated image.

After the patient with bilateral hip prostheses was CT scanned, the DICOM image files were processed by a stand-alone application program utilizing the smoothing-plus-scaling metal artefact suppression technique (Wei *et al* 2004). Then the two CT image sets, before metal artefact suppression and after, were input to the treatment planning system. Fictitious circular-shaped tumours and organs at risk were contoured. The same contour information and beam set-up were applied to each CT image set by either duplicating the contour files and beam configuration files or using the same treatment planning parameters. CT numbers were converted to electron density based on the calibration curve clinically used for radiation treatment planning. For proton and electron beams, treatment planning was performed on a CMS XiO system (CMS, Inc., St. Louis, MO) and tissue inhomogeneity correction was turned on for the dose calculations. Photon beam treatment planning was performed on an ADAC Pinnacle3 system (Philips Medical Systems, Bothell, WA). In this case, dose calculations with and without inhomogeneity corrections were generated and compared. Isodose curves, dose volume histograms (DVH) and target/OAR dose statistics were used as the basis for the dose distribution comparisons.

The treatment plans presented in this paper are chosen to illustrate the dosimetric impact of severe metal artefacts and the potential advantage of our previously published artefact suppression algorithm (Wei *et al* 2004). By performing example dose calculations based on CT images severely contaminated with metal artefacts, there is no intended inference that such dose calculations are currently performed in clinical practice on severely contaminated CT images without some form of mitigation or correction before the resultant dose distribution is accepted for patient treatment.
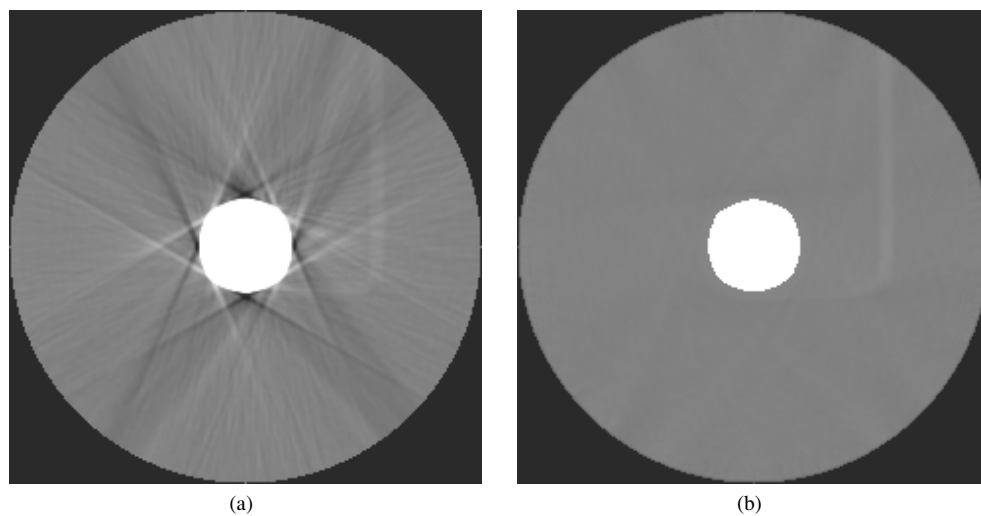
Figure 1. Water phantom with a metal rod inserted (a) before artefact suppression and (b) after artefact suppression.

Table 1. Mean CT number values and the CT number standard deviation values of (a) the difference image of one slice of homogeneous water subtracted by an adjacent slice, (b) the difference image of homogeneous water minus the artefact-contaminated image, (c) and the difference image of homogeneous water minus the artefact-suppressed image.

	Water − water (a)	Water − artefact contaminated (b)	Water − artefact suppressed (c)
Mean (HU)	0.5	0.7	1.0
Std. dev. (HU)	16.5	60.2	20.2

3. CT number accuracy

To analyse how accurate the CT numbers are after the image processing, a water phantom with a metal rod in the centre was scanned. The CT scanning peak voltage was 120 kVp. The metal rod used was an alloy made of cobalt–chromium–molybdenum (Co: 63–68%, Cr: 27–30%, Mo: 5–7%) having a diameter of 3 cm. The original image with the metal rod is shown in figure 1(a), and the processed image in figure 1(b). The mean CT numbers and standard deviations for three difference images are listed in table 1. The pixels due to the metal rod are excluded in calculating the mean and standard deviations. The second column (water − water) of table 1 is the mean value and standard deviation of the difference image obtained by subtracting the image of one slice of homogeneous water from an adjacent slice. The third column is the mean value and standard deviation of the difference image of homogeneous water and the artefact contaminated image. The fourth column is the mean value and standard deviation of the difference image of homogeneous water and the artefact suppressed image. The standard deviation of CT numbers in the water − water difference image is due to noise. The standard deviation of CT number in the water − artefact-suppressed image (20.2 HU) is much lower than that for the water − artefact-contaminated image (60.2 HU) but close to the water − water image noise (16.5 HU). This result demonstrates that the image processing procedure is able to suppress the metal artefacts significantly while keeping image noise almost as low as the intrinsic image noise produced by the scanner.

It is noted that the shape of the metal rod in the transverse CT slices (both figures 1(a) and (b)) is an octagon instead of a perfect circle. The change in shape is part of the artefacts created by the high-density metal rod. This specific part of the metal artefacts is not suppressed by the smoothing-plus-scaling algorithm (Wei *et al* 2004) which is most effective in suppressing bright and dark streak artefacts spread over the CT image. However, as discussed in section 1, treatment planners usually do their best to avoid having beams pass through the high-density objects. In this paper, all dose distributions studied are not dependent on the accurate shape information of the metal objects. Therefore, the shape change does not compromise the validity of the study and conclusions in this paper.

4. Case study for proton therapy

The CT images used in this study were obtained for a patient with bilateral hip prostheses that led to severe metal artefacts appearing in the CT images. The artefacts appear mainly as dark streaks and are severe in the centre region overlapping with normal tissues such as the bladder, rectum and prostate. A fictitious circular-shaped tumour was contoured on each slice, as shown in purple colour in figures 2(a) and (b). A single proton beam of energy 150 MeV was planned to deliver a 1000 cGy dose to the centroid of the tumour. The CMS XiO treatment planning system was used for calculations. Based on the metal artefact-contaminated CT image set, treatment planning was performed to achieve good coverage of the tumour's distal edge. The beam compensator and range modulator were selected so that the beam range was 15.82 cm and the spread out Bragg peak (SOBP) was 5.10 cm wide. The dose distribution normalized to 1000 cGy was calculated (figure 2(a)) as well as the dose volume histogram (DVH) (figure 2(c)). The 95% isodose line of figure 2(a) fails to cover the tumour distal edge perfectly due to the noisy density information in the artefact region and the limited spatial resolution of the beam compensators designed at MPRI (Midwest Proton Radiotherapy Institute).

The same beam energy, compensator and range modulator were then applied to the artefact-suppressed image set. The resulting dose distribution is shown in figure 2(b) and the DVHs compared in figure 2(c). The distal portion of the isodose lines is shifted upstream towards the source demonstrating that a treatment based on the artefact-contaminated images would cause the tumour to be severely underdosed. This severe tumour underdosage is quantified by the DVH graphs in figure 2(c).

Figures 3(a) and (b) show the dose distribution and DVH when the compensator is designed using the artefact-suppressed image set. The target coverage is smoother in figure 3(a) than in figure 2(a) and the DVH in figure 3(b) is as good as in figure 2(c) (solid line). For this case, the beam compensator and range modulator were selected so that the beam range was 17.13 cm and the spread out Bragg peak (SOBP) was 6.0 cm wide.

Proton beam distributions are highly sensitive to tissue density encountered along the beam's path. This is the primary reason severe underdosage or overdosage of a tumour is possible when treatment planning is performed using a metal artefact-contaminated image.

5. Case study for electron therapy

For the same patient images discussed in section 4, a 21 MeV electron beam of field size 5 cm × 5 cm and SSD 100 cm was applied to deliver 1000 monitor units of radiation to a region in the proximity of one of the two metal implants where both bright and dark artefacts are present. The beam angle was chosen to be 50°, approximately perpendicular to the patient surface and the dose grid size was chosen to be 0.5 cm. A dose distribution based on the
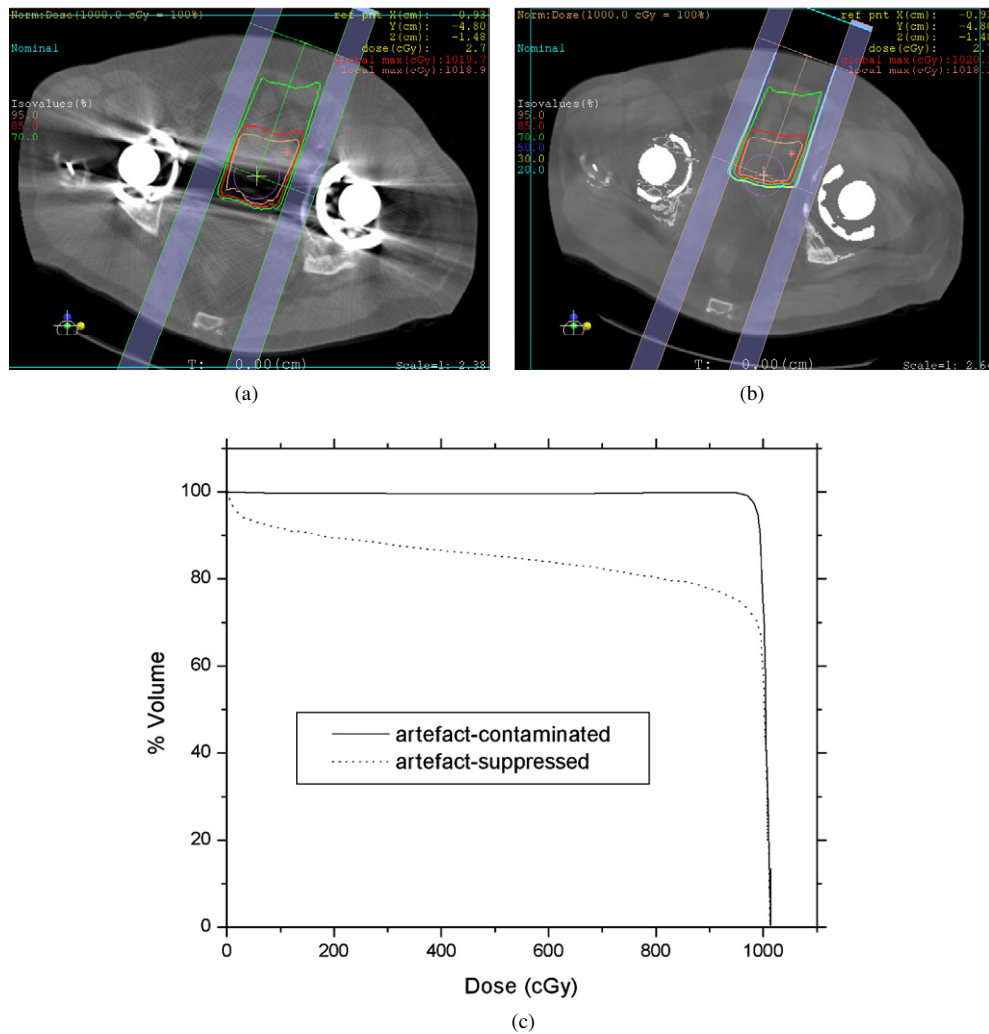
(a)   (b)

(c)

Figure 2. (a) Dose distribution when a single proton beam of energy 150 MeV was planned to deliver a 1000 cGy dose to the centroid of the tumour based on the artefact-contaminated image. The beam range was 15.82 cm and the spread out Bragg peak (SOBP) was 5.10 cm wide. (b) Dose distribution when the same beam energy, compensator and range modulator were applied to the artefact-suppressed image. (c) Dose volume histograms for both (a) and (b). The isodose lines are marked in colour as follows: 95% in orange, 85% in red, 70% in green.

artefact-contaminated image is shown in figure 4(a), and compared to that based on the artefact-suppressed in figure 4(b). In both figures, the absolute isodose curves are drawn for 1000, 900, 800, 500 and 300 cGy. Comparing figures 4(a) and (b), the shape of the 1000 cGy isodose line and the location of the maximum dose point, marked by an asterisk, are different. In figure 4(b), the isodose lines within the field are perpendicular to the central axis, while those in figure 4(a) are tilted. This is because the beam dose calculations predict a greater depth of penetration when the tissue density is fictitiously lowered by the metal artefacts. The depths of the 900 cGy and 500 cGy isodose lines for both figures are measured along the central axis and listed in table 2.
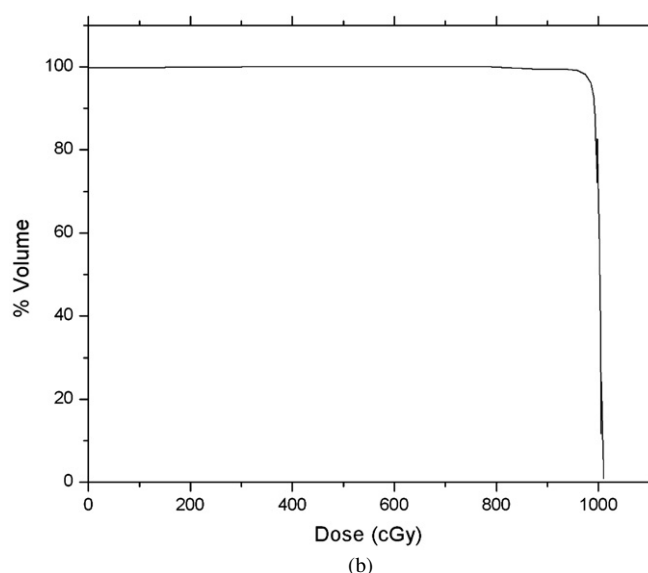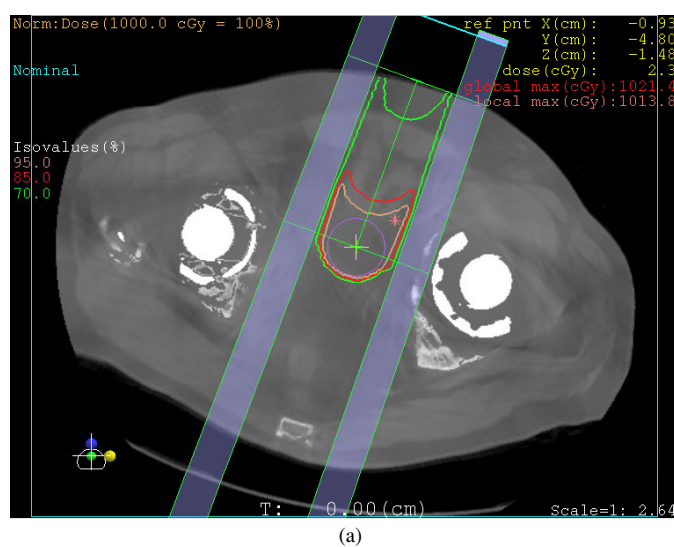
(a)

(b)

Figure 3. (a) Dose distribution when a single proton beam of energy 150 MeV was planned to deliver a 1000 cGy dose to the centroid of the tumour based on the artefact-suppressed image. The beam range was 17.13 cm and the spread out Bragg peak (SOBP) was 6.0 cm wide. (b) Dose volume histogram for (a). The isodose lines are marked in colour as follows: 95% in orange, 85% in red, 70% in green.

The depth difference of the 900 cGy isodose lines between figures 4(a) and (b) indicates that dose predictions for the electron beam assume greater electron energy loss based on the artefact-contaminated image because the beam passes through a bright artefact region of fictitious high density tissue. The depth difference of the 500 cGy isodose lines indicates the opposite because the beam passes through a dark artefact region of fictitious low density tissue. This fictitious low density tissue effect is great enough to not only counteract the fictitious high density effect due to bright artefacts but also results in a net increase in the depth
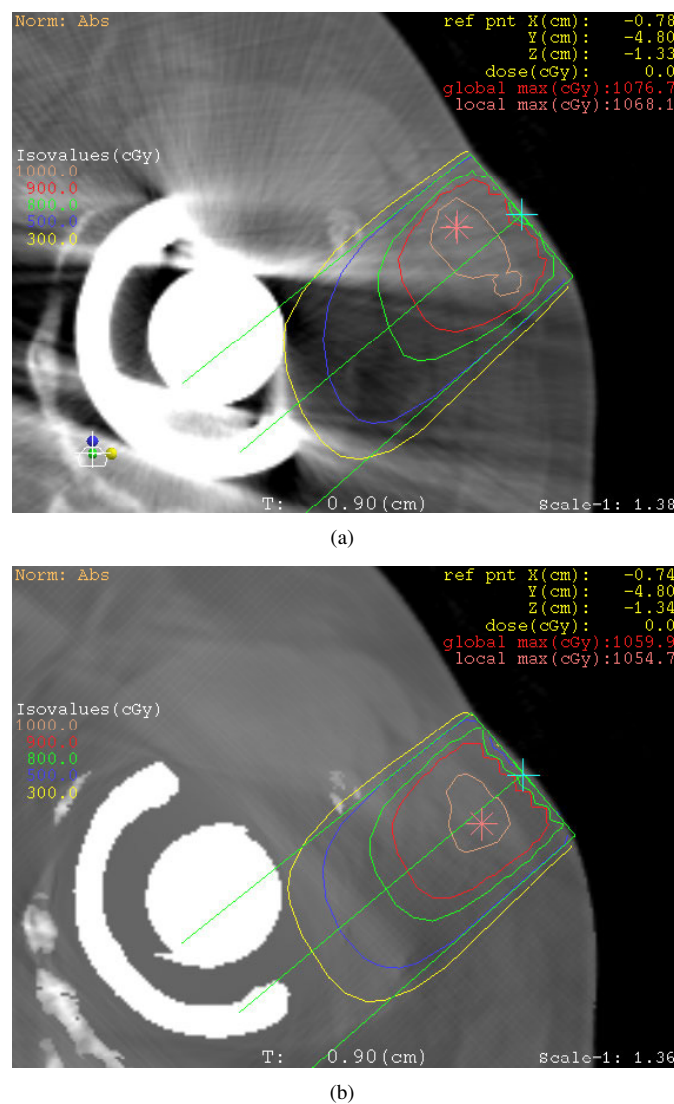
(a)

(b)

Figure 4. (a) Absolute dose distribution when a 21 MeV electron beam of field size 5 cm × 5 cm and SSD 100 cm was applied to deliver 1000 monitor units of radiation based on the artefact-contaminated image. (b) Absolute dose distribution when the same 21 MeV electron beam of field size 5 cm × 5 cm and SSD 100 cm was applied to deliver 1000 monitor units of radiation based on the artefact-suppressed image. The isodose lines are marked in colour as follows: 1000 cGy in orange, 900 cGy in red, 800 cGy in green, 500 cGy in blue, 300 cGy in yellow.

that the beam can reach. The above differences demonstrate the deviation in dose distribution that one should expect if a metal artefact-contaminated image is used for treatment planning and the computed monitor units based on this contaminated image are used for the actual treatment.

Following clinical practice, the dose values in figures 4(a) and (b) were then normalized to their respective dose maxima to obtain the dose distributions shown in figures 5(a) and (b). The 95% and 90% isodose lines in figure 5(a) are different in shape from those in
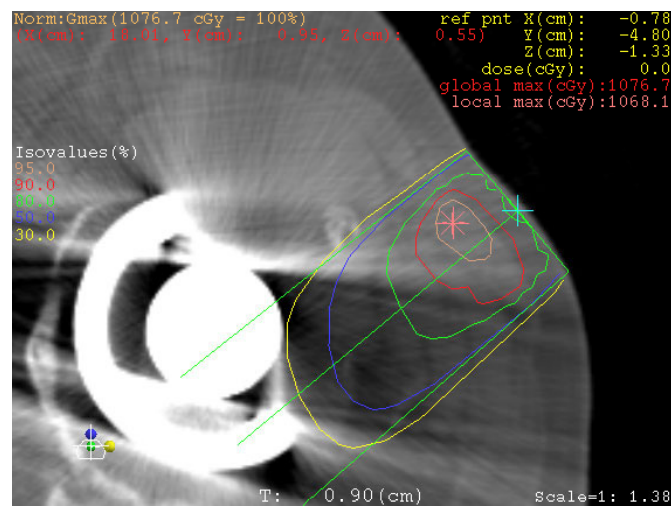
(a)
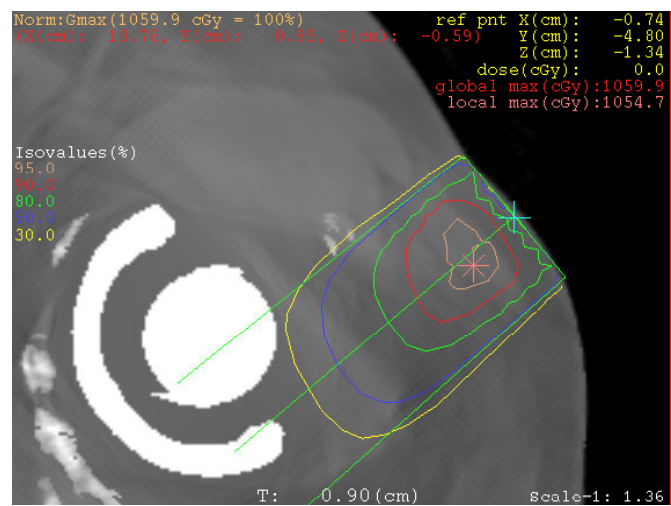
(b)

Figure 5. Percentage isodose curves when the dose values in figures 4(a) and (b) were normalized to their respective dose maxima (a) based on the artefact-contaminated image, (b) based on the artefact-suppressed image. The isodose lines are marked in colour as follows: 95% in orange, 90% in red, 80% in green, 50% in blue, 30% in yellow.

Table 2. Depths of the distal ends for isodose lines measured along the central axis.

|		Depth (cm)	
		Artefact-contaminated image	Artefact-suppressed image
Absolute	900 cGy	4.27	4.60
isodose	500 cGy	7.86	7.38
Percentage	90%	3.33	3.92
isodose	50%	7.50	7.26
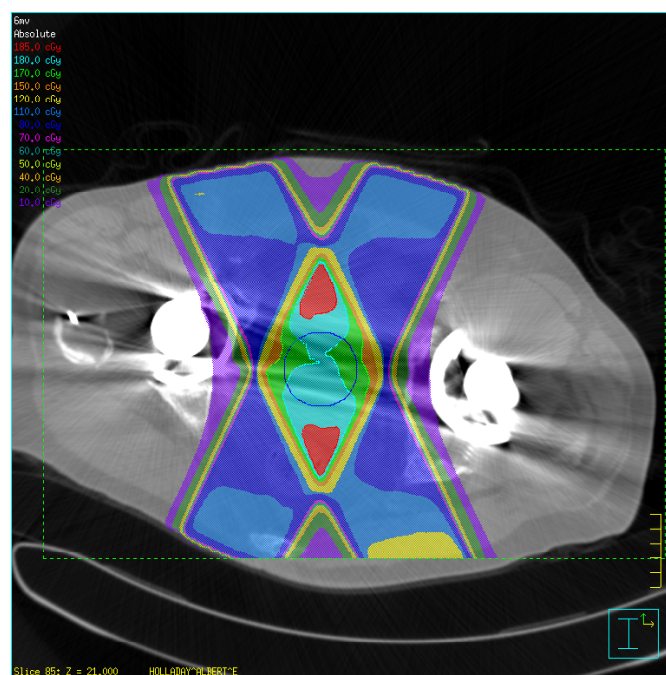
(a)
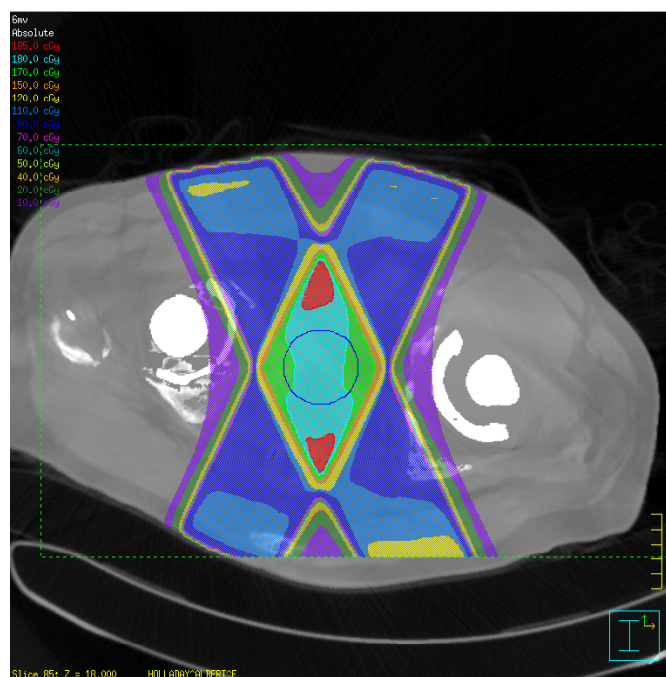
(b)

Figure 6. Isodose curves for a four-beam 6 MV photon treatment based on (a) an artefact-contaminated image and (b) an artefact-suppressed image. The isodose lines are marked in colour as follows: 185 cGy in red, 180 cGy in cyan, 170 cGy in green, 150 cGy in orange, 120 cGy in yellow.
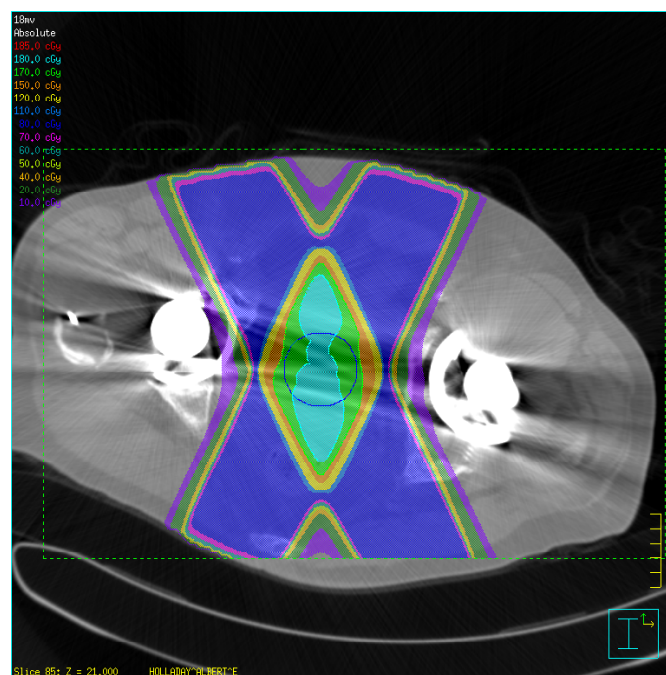
(a)
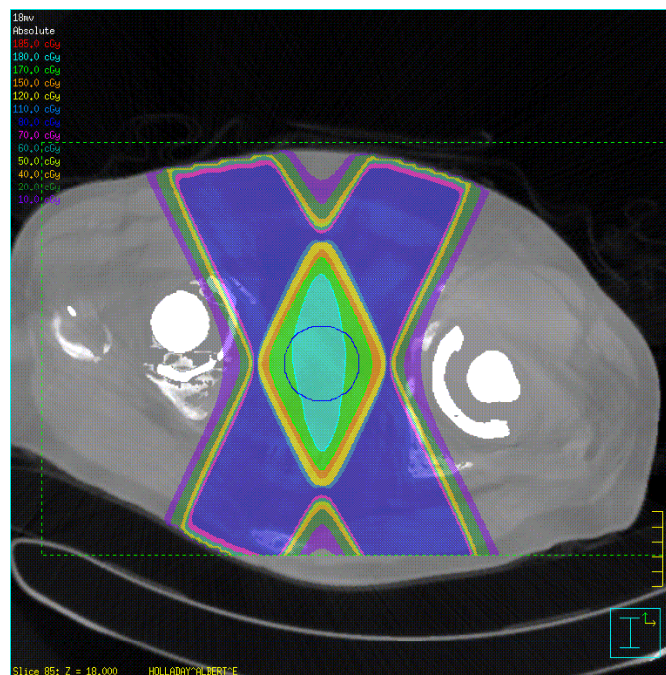
(b)

Figure 7. Isodose curves for an 18 MV photon beam based on (a) an artefact-contaminated image and (b) an artefact-suppressed image. The isodose lines are marked in colour as follows: 185 cGy in red, 180 cGy in cyan, 170 cGy in green, 150 cGy in orange, 120 cGy in yellow.
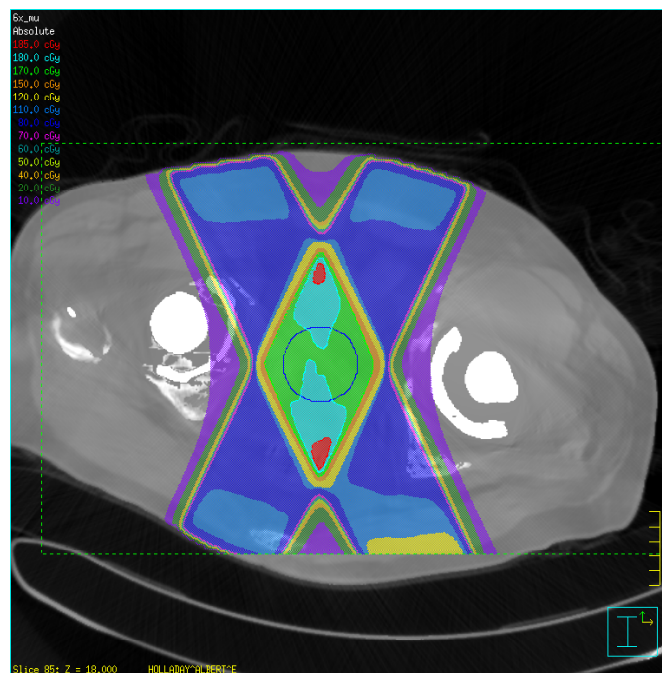
Figure 8. Based on the artefact-suppressed image with the inhomogeneity correction turned on, the monitor units obtained by treatment planning based on the artefact-contaminated image set are applied to the artefact-suppressed image set. The isodose lines are marked in colour as follows: 185 cGy in red, 180 cGy in cyan, 170 cGy in green, 150 cGy in orange, 120 cGy in yellow.

figure 5(b), similar to the situation in figures 4(a) and (b). Clinically, these isodose lines are often prescribed to cover the tumour volume. As listed in table 2 the central axis 90% isodose line reaches a shallower depth and the 50% isodose line reaches a greater depth when dose calculations are performed on the artefact-contaminated image. These deviations will be typical of the treatment planning errors introduced when using an artefact-contaminated image.

6. Case study for photon therapy

For the same patient images discussed in section 4, a 5 cm diameter circular-shaped tumour was contoured and made the same shape and dimension on each slice. The centre of the circular tumour in the middle of the irradiated volume was selected to be the isocentre. Four equally weighted and parallel opposed photon beams were planned to deliver a 180 cGy dose to the isocentre using either a set of 6 MV or 18 MV photon beams.

Figure 6 shows the dose distributions of one CT slice for the 6 MV photon beam treatment based on the artefact-contaminated and artefact-suppressed CT image sets with the inhomogeneity correction turned on. Comparing the dose distributions in figures 6(a) and (b), we see that the 170 cGy isodose line (marked green) on the artefact-suppressed image (figure 6(b)) has a more regular diamond shape than that of the artefact-contaminated image (figure 6(a)). The 180 cGy isodose line (marked cyan) of the artefact-contaminated image (figure 6(a)) has an irregular shape and the tumour is severely
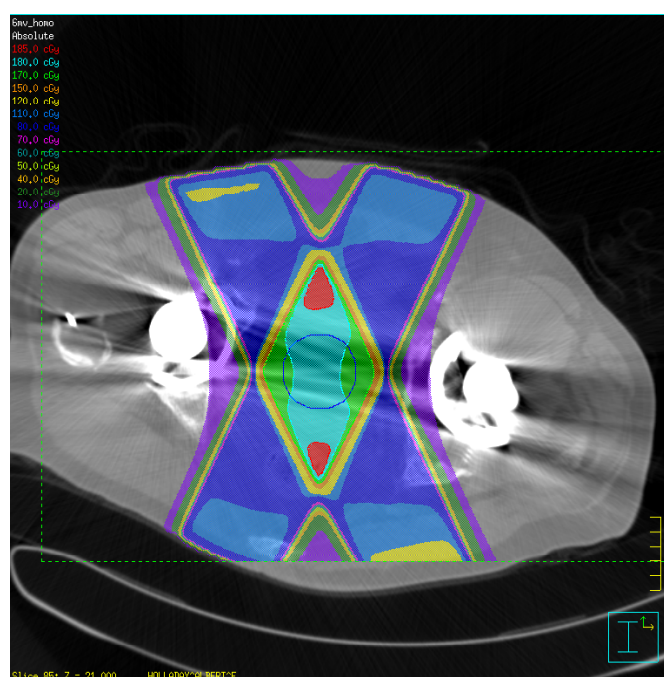
Figure 9. Based on the artefact-contaminated image but with the dose inhomogeneity correction turned off, four 6 MV photon beams are applied to deliver a dose of 180 cGy to the fictitious circular shaped tumour in the centre. The isodose lines are marked in colour as follows: 185 cGy in red, 180 cGy in cyan, 170 cGy in green, 150 cGy in orange, 120 cGy in yellow.

underdosed while figure 6(b) shows that the same isodose line based on the artefact-suppressed images has a smoother boundary and covers a larger area of the target. The 185 cGy isodose line (marked red) in figure 6(b) covers a smaller area than that in figure 6(a). These differences are attributed to the photon scattering at the fictitious inhomogeneity interfaces introduced by the severe dark streak artefacts and the resulting fictitious low-density tissue leading to reduced attenuation predictions for the photon beam.

Figures 7(a) and (b) show the dose distributions on the same CT slices for a four-beam 18 MV photon treatment based on both the artefact-contaminated and artefact-suppressed CT image sets with the inhomogeneity correction turned on. Compared to 6 MV beams, the dose distributions for the 18 MV photon beams are less affected by the metal artefacts due to the higher energy beam being less sensitive to the scattering at low density inhomogeneity interfaces.

The isodose comparisons made were based on the condition that the isocentre should receive 180 cGy no matter which image set is used. However, it is also of interest to consider the impact on monitor unit calculations for an artefact-contaminated image. We therefore applied the same monitor units used in the planned treatment represented by figure 6(a) based on the artefact-contaminated image set but this time applied them to the artefact-suppressed image set. Figure 8 shows that, overall, the dose level is lower than that in figure 6(a) and the target would therefore be underdosed compared to the planned dose.

Figure 9 shows the dose distribution of the same CT slice for 6 MV beams based on the artefact-contaminated CT image set but with the inhomogeneity correction turned off. (That

is, the volume of interest is treated by the dose calculation algorithm as homogeneous water.) We observed that the dose distributions look similar to those based on the artefact-suppressed image set except that the size and shape of the isodose regions are slightly different. This difference should be attributed to the fact that the region of interest is treated as homogeneous water without any inhomogeneity dose calculation correction. From this limited case study, it seems that if no CT metal artefact suppression method was available to the treatment planner, then in the cases of severe artefacts and photon beam treatments turning off the inhomogeneity correction when performing dose calculations may reduce dose calculation errors.

7. Conclusion

The CT number analysis of the scanned water phantom with inserted metal rods demonstrated that the previously proposed CT metal artefact suppression method can faithfully reproduce the CT numbers of tissues that are overlapped by the artefacts. The CT number standard deviation of the difference image obtained by subtracting the processed image from the metal-free image is roughly comparable to the typical standard deviation of the CT image of a homogeneous medium.

We studied the dosimetric effect of the previously proposed CT metal artefact suppression method for proton, electron and photon beams. CT image sets of a patient case with bilateral hip prostheses before and after artefact suppression were input to the treatment planning system for comparison. Dose distributions for all beam types were found to be affected in terms of the isodose curves and dose volume histograms computed. For all beam types, beam angles were chosen so that direct irradiation of the metal implants was avoided. If treatment planning is based on an artefact-contaminated CT image set, the actual dose delivered to a target can be considerably less than that planned and organs at risk may be overdosed.

The cumulative tissue density met by a proton beam is the primary determining factor for dose distribution changes. Therefore the response of a proton beam to CT image metal artefact removal is the most predictable of the beam types studied. Photon and electron beams are affected by both tissue density and scattering due to atomic number differences between tissues. Removal of dark streak artefacts, that had introduced fictitious low density tissue as input to the dose calculations, has the effect of pulling the computed isodose lines upstream towards the radiation source.

CT metal artefact suppression plays an important role in improving radiation treatment planning dose calculations, especially for patients with large metal implants.

Acknowledgment

References

Constantinou C, Harrington J C and DeWerd L A 1992 An electron density calibration phantom for CT-based treatment planning computers *Med. Phys.* **19** 325–7
Coolens C and Childs P J 2003 Calibration of CT Hounsfield units for radiotherapy treatment planning of patients with metallic hip prostheses: the use of the extended CT-scale *Phys. Med. Biol.* **48** 1591–603
Ding G X and Yu W 2001 A study on beams passing through hip prosthesis for pelvic radiation treatment *Int. J. Radiat. Oncol. Biol. Phys.* **51** 1167–75
Goitein M 1978 A technique for calculating the influence of thin inhomogeneities on charged particle beams *Med. Phys.* **5** 258–64

Guan H, Yin F-F and Kim J H 2002 Accuracy of inhomogeneity correction in photon radiotherapy from CT scans with different settings *Phys. Med. Biol.* **47** N223–31

Henson P W and Fox R A 1994 The electron density of bone for inhomogeneity correction in radiotherapy planning using CT numbers *Phys. Med. Biol.* **29** 351–9

Mustafa A A and Jackson D F 1983 The relation between x-ray CT numbers and charged particle stopping powers and its significance for radiotherapy treatment planning *Phys. Med. Biol.* **28** 169–76

Parker R P, Hobday P A and Cassell K J 1979 The direct use of CT numbers in radiotherapy dosage calculations for inhomogeneous media *Phys. Med. Biol.* **24** 802–9

Perry D J and Holt J G 1980 A model for calculating the effects of small inhomogeneities on electron beam dose distributions *Med. Phys.* **7** 207–15

Roberts R 2001 How accurate is a CT-based dose calculation on a pencil beam TPS for a patient with a metallic prosthesis? *Phys. Med. Biol.* **46** N227–34

Schneider U, Pedron E and Lomax A 1996 The calibration of CT Hounsfield units for radiotherapy treatment planning *Phys. Med. Biol.* **41** 111–24

Szymanowski H and Oelfke U 2003 CT calibration for two-dimensional scaling of proton pencil beams *Phys. Med. Biol.* **48** 861–74

Thomadsen B R, Paliwal B R, Laursen J F, Filamor C O and van de Geijn P 1983 Some phantom designs for radiation dosimetry and CT applications *Med. Phys.* **10** 886–8

Wei J, Chen L, Sandison G A, Liang Y and Xu L X 2004 X-ray CT high-density artifact suppression in the presence of bones *Phys. Med. Biol.* **49** 5407–18

Wieslander E and Knoos T 2003 Dose perturbation in the presence of metallic implants: treatment planning system versus Monte Carlo simulations *Phys. Med. Biol.* **48** 3295–305